

Time-dependent photospheric radiative transfer in structured GRB jets: spectral evolution and polarization diagnostics

YUE XU,^{1,2} MING JIN,³ AND QINGWEN TANG¹

¹*Department of Physics, School of Physics and Materials Science, Nanchang University, Nanchang 330031, China*

²*Henan Institute for Drug and Medical Device Control, Zhengzhou 450018, China*

³*Shanghai Johnson & Johnson Pharmaceuticals, Ltd., Shanghai, China*

ABSTRACT

Photospheric emission from relativistic gamma-ray burst (GRB) jets is a promising mechanism for producing the Band-like spectra observed in the prompt phase, yet the connections between jet structure, dissipation location, and polarization signatures remain unclear. We investigate time-dependent photospheric radiation transfer in structured relativistic jets by coupling two-dimensional axisymmetric special relativistic hydrodynamic (SRHD) simulations with Monte Carlo photon propagation.

Photon escape and subphotospheric dissipation are characterized using the residual line-of-sight optical depth $\tau_{\text{out}}(\hat{\Omega})$ evaluated along each photon trajectory, allowing a direction-dependent treatment of photon decoupling in structured jets. The radiative transfer includes Klein–Nishina Compton scattering and polarization evolution using the Mueller matrix formalism.

We perform a systematic parameter study exploring the effects of viewing angle, electron–positron pair loading (Z_{\pm}), and the optical-depth window of subphotospheric dissipation. The model produces time-resolved spectra, peak-energy evolution $E_{\text{pk}}(t)$, Band parameters, polarization degree $\Pi(E, t)$, and last-scattering statistics.

We find that jet angular structure and the geometry of the line-of-sight optical depth strongly regulate spectral evolution and polarization signatures. The dissipation depth and pair loading jointly control the stability of E_{pk} , the formation of high-energy spectral tails, and the energy dependence of polarization. These results provide quantitative predictions for GRB prompt-emission spectra and polarization that can be tested with current and upcoming high-energy polarimeters..

Keywords: gamma-ray bursts — radiative transfer — relativistic processes — polarization

1. INTRODUCTION

Gamma-ray bursts (GRBs) are among the most luminous transient phenomena in the Universe. During the prompt-emission phase, typically observed in the ~ 10 keV–10 MeV band, the spectra are commonly described by the empirical Band function and exhibit pronounced temporal evolution (Band et al. 1993; Kaneko et al. 2006; Axelsson & Borgonovo 2015). In particular, the peak energy E_{pk} often evolves in correlation with the flux, while the low-energy spectral index α and the high-energy tail vary across individual pulses. These time-resolved spectral properties provide important con-

straints on the radiation mechanisms operating in relativistic GRB jets (Piran 2004; Mészáros 2006).

In addition to spectral diagnostics, polarization measurements offer an independent probe of jet geometry and radiation physics. The polarization degree Π and polarization angle χ are sensitive to the anisotropy of the radiation field, the geometry of the visible emitting region, and the underlying emission or scattering processes. Consequently, polarization can help distinguish between competing prompt-emission scenarios that produce similar spectral signatures. Recent observations with POLAR and AstroSat/CZTI have reported statistically significant linear polarization in several GRBs (Kole et al. 2020; Chattopadhyay et al. 2019, 2022), motivating theoretical studies that simultaneously address spectral formation and polarization in relativistic outflows.

1.1. Photospheric emission in structured jets

If radiation is produced at sufficiently high optical depth in an ultra-relativistic outflow, photons undergo multiple scatterings before escaping, naturally leading to photospheric emission (Paczynski 1986; Goodman 1986). In the simplest fireball picture, radiation and plasma approach thermal equilibrium at $\tau \gg 1$, producing quasi-thermal spectra near a blackbody or Wien peak. However, in realistic GRB jets the photon decoupling process is intrinsically stochastic and does not occur at a sharply defined geometric radius. Instead, the photosphere corresponds to a statistical last-scattering region whose spatial distribution depends on the local velocity field, density structure, and photon propagation direction (Pe’er 2008; Beloborodov 2011).

Furthermore, GRB jets are unlikely to be angularly uniform. Hydrodynamic simulations and observational modeling suggest that relativistic jets possess substantial angular structure, such as core–sheath configurations or velocity shear with continuous variations in $\Gamma(\theta)$ and $\rho(\theta)$. In such structured outflows, photons emitted from different angular regions contribute differently to the observed signal. Off-axis viewing introduces variations in Doppler boosting, equal-arrival-time-surface (EATS) effects, and geometric asymmetry of the visible region, which can jointly influence the observed spectral evolution and polarization signatures (Lundman et al. 2013). Photospheric emission in structured jets therefore constitutes a coupled radiative-transfer problem in which spectral formation and polarization both depend sensitively on jet geometry and scattering physics.

1.2. Monte Carlo radiative transfer in relativistic jets

Theoretical studies of GRB photospheric emission generally follow two complementary approaches. One approach employs radiation hydrodynamics or moment-based formalisms that evolve angular moments of the radiative transfer equation together with the fluid dynamics. Such treatments provide valuable insight into the global evolution of radiation and plasma under quasi-steady conditions (Beloborodov 2010; Vurm & Beloborodov 2016), but become increasingly complex when strong angular inhomogeneity, non-local scattering, or polarization effects are included.

An alternative approach is to perform photon Monte Carlo simulations on top of a prescribed hydrodynamic background. By explicitly tracking individual photon trajectories and scattering histories, this method naturally captures direction-dependent transport, non-local scattering, and polarization evolution, while directly producing observable quantities such as time-resolved spectra and polarization signals (Ito et al. 2013; San-

tana et al. 2014; Parsotan & Lazzati 2023). The main limitation of this approach is that radiative feedback on the fluid dynamics is neglected.

In this work, we adopt the Monte Carlo approach and extend it to treat time-dependent radiative transfer in structured relativistic jets. We first perform two-dimensional axisymmetric special relativistic hydrodynamic (SRHD) simulations to obtain time-resolved jet backgrounds. Photons are then propagated through successive simulation snapshots using a piecewise-constant-in-time approximation, allowing photon propagation delays to accumulate and enabling the construction of time-resolved spectra and polarization signals.

A key aspect of our method is the treatment of photon decoupling in structured jets. Rather than defining the photosphere using a purely radial optical-depth coordinate, we compute the residual optical depth along the actual photon propagation direction, $\tau_{\text{out}}(\hat{\Omega})$, defined as the remaining Thomson optical depth integrated along the photon trajectory toward the observer. We adopt this quantity as the fundamental coordinate for photon escape and subphotospheric dissipation. This coordinate naturally incorporates geometric effects arising from jet structure and viewing angle, and provides a unified description of the decoupling process in anisotropic outflows (Pe’er 2008; Beloborodov 2011; Lundman et al. 2013; Ito et al. 2013).

Within this framework, we present a time-dependent Monte Carlo radiative-transfer model for photospheric emission in structured relativistic jets and investigate its observable implications. Our main results can be summarized as follows. (i) We show that a structured SRHD jet background without additional dissipation or pair loading naturally produces quasi-thermal spectra with limited spectral broadening, providing a baseline for interpreting GRB prompt-emission spectra. (ii) By introducing a parameterized subphotospheric dissipation window ($\tau_{\text{diss,min}}, \tau_{\text{diss,max}}$), we demonstrate that the depth of dissipation strongly regulates the formation of high-energy spectral tails and the evolution of the peak energy E_{pk} . (iii) We quantify how electron–positron pair loading, parameterized by Z_{\pm} , modifies the effective optical depth, spectral peak energy, and polarization signatures. (iv) We show that the viewing angle θ_{obs} significantly affects light-curve morphology, time-resolved $E_{\text{pk}}(t)$ evolution, and polarization observables due to geometric and Doppler effects in structured jets. (v) We examine the sensitivity of the results to numerical factors such as snapshot cadence, escape criteria, and spatial resolution, providing guidance for interpreting Monte Carlo simulations of photospheric emission.

The paper is organized as follows. Sections 3 and 4 describe the SRHD simulations and the Monte Carlo radiative-transfer method. Section 5 presents the parameter study, and Section 6 summarizes the implications and limitations of the model.

2. PHOTOSPHERIC MODEL AND NUMERICAL RADIATIVE TRANSFER

In this section we summarise the multi-zone physical picture of dissipative photospheres (Planck/Wien/unsaturated Comptonization zones) and the role of electron–positron pair loading in regulating the effective optical depth, thereby motivating the expected behaviour of the peak energy E_{pk} , spectral broadening, and polarization signatures. We then clarify the positioning of our numerical approach relative to analytic radiation-hydrodynamic treatments: rather than solving moment equations with closure relations or performing fully self-consistent radiation–fluid coupling, we post-process time-resolved outputs from a two-dimensional axisymmetric special relativistic hydrodynamic (SRHD) jet simulation using a photon-by-photon Monte Carlo radiative transfer scheme. In this framework, the residual line-of-sight optical depth defined along the true propagation direction, $\tau_{\text{out}}(\hat{\Omega})$, is adopted as a unified criterion for photon decoupling and as the coordinate that parameterizes subphotospheric dissipation, enabling a consistent treatment of direction-dependent optical depth effects in structured jets under off-axis geometries. Temporally, we employ a time-dependent treatment in which the background is approximated as piecewise frozen, allowing photons to propagate and scatter across multiple SRHD snapshots while accumulating light-travel-time delays, so as to produce time-resolved spectral and polarization diagnostics.

2.1. Multi-zone photospheric structure and subphotospheric dissipation

In dissipative photospheric models, an outflow expands from optically thick regions to transparency. The coupling between radiation and plasma varies continuously with radius, but different physical processes dominate in different regimes (Paczynski 1986; Goodman 1986; Pe’er 2008; Beloborodov 2010; Vurm & Beloborodov 2016):

1. **Planck zone** ($\tau_{\text{T}} \gtrsim 10^5$): double Compton and free–free emission are efficient, so both photon number and energy approach local thermal equilibrium, yielding a nearly blackbody spectrum. The outflow evolution in this regime is well approximated as adiabatic expansion.

Schematic structure of GRB photosphere

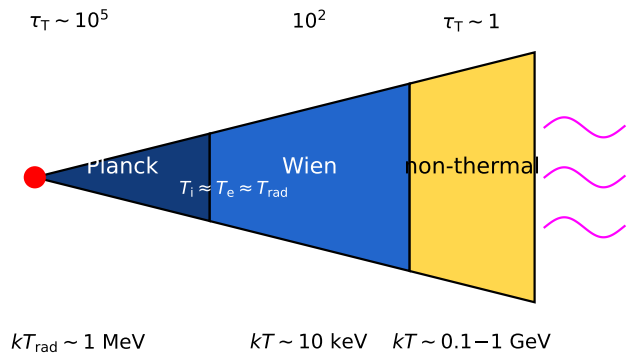


Figure 1. Schematic illustration of a multi-zone dissipative photosphere and the concept of the line-of-sight optical-depth coordinate. The horizontal axis denotes radius r , indicating the Planck, Wien, and unsaturated Comptonization zones. In structured jets, photon decoupling is more naturally characterised by the residual optical depth along the true propagation direction, $\tau_{\text{out}}(\hat{\Omega})$, rather than by a single radial optical-depth profile $\tau(r)$.

2. **Wien zone** ($10^2 \lesssim \tau_{\text{T}} \lesssim 10^5$): the Compton y -parameter satisfies $y \gg 1$, maintaining Compton equilibrium between radiation and electrons. The spectrum approaches a narrow Wien shape (allowing a non-zero chemical potential). The photon number effectively freezes out near the so-called Wien radius R_{W} , which largely sets the eventual peak energy E_{pk} .
3. **Unsaturated Comptonization zone** ($1 \lesssim \tau_{\text{T}} \lesssim 10^2$): subphotospheric dissipation continuously heats electrons (including e^{\pm} pairs), reducing the Compton y -parameter to $\mathcal{O}(1)$. A non-thermal high-energy tail develops, while repeated scatterings shape the low-energy spectrum toward a Band-like slope with $\alpha \sim -1$ (Beloborodov 2010; Vurm & Beloborodov 2016).

The peak energy E_{pk} is primarily controlled by the ratio of radiation energy density to photon number set in the Planck/Wien zones, whereas spectral broadening, the formation of non-thermal tails, and the evolution of the low-energy slope mainly occur in the unsaturated Comptonization regime at $\tau_{\text{T}} \sim 1\text{--}10^2$. Because the last-scattering radius typically spans a broad range, $\sim 0.3R_{\text{ph}}\text{--}3R_{\text{ph}}$, the photosphere is not a geometrically sharp surface but an extended decoupling region in a statistical sense (Pe’er 2008; Beloborodov 2011). In structured jets viewed off-axis, the shape of this decoupling region depends on the viewing direction, thereby

imprinting measurable effects on both spectral and polarization properties.

2.2. *Electron–positron pair production and optical-depth self-regulation*

Within the subphotospheric dissipation region, photon–photon collisions can trigger $\gamma + \gamma \rightarrow e^+ + e^-$, substantially increasing the local lepton density. This process has been recognised since early GRB theory as an important ingredient of dissipative outflows (Rees & Mészáros 1994; Thompson 1994; Mészáros & Rees 2000). It is convenient to introduce a pair-loading factor, $Z_{\pm} \equiv n_{\pm}/n_p$, to quantify the enhancement of the lepton number density relative to protons.

Numerical studies indicate that Z_{\pm} can reach $\sim 10^2$ in radiation-mediated shock fronts and then decrease downstream due to pair annihilation (Levinson & Nakar 2020). The MeV photons required for pair creation may arise from bulk Comptonization associated with velocity shear, and may also be produced by inverse-Compton scattering of hot electrons if collisionless substructures develop within the shock transition.

Sustained e^{\pm} production can strongly modify the effective optical depth. Even if the background electron–proton plasma would otherwise become transparent, a dissipative layer may remain at $\tau_T \gtrsim 1$ due to pair loading, keeping radiation coupled to the plasma out to larger radii (Beloborodov 2017; Ito et al. 2013). In this case the photosphere is no longer associated with a fixed radius; rather, it is effectively “carried” outward by the pair-supported dissipative layer as the jet expands.

We stress that, in principle, the spatial distribution of Z_{\pm} should be determined self-consistently by the radiation field together with pair creation and annihilation microphysics. Here our aim is to quantify the sensitivity of observable diagnostics to pair loading in a parameterised manner. We therefore treat Z_{\pm} as an external control parameter and scan its values in numerical experiments. Its primary impact is to regulate the effective optical depth and the geometry of the last-scattering surface, thereby shaping the responses of E_{pk} , spectral form, and polarization to pair loading.

2.3. *Line-of-sight optical depth in structured jets*

In spherically symmetric, steady outflows, the radial optical depth $\tau(r)$ is often used as an approximate “photospheric coordinate”, from which a photospheric radius R_{ph} can be defined. In structured jets, however, both density and Lorentz factor vary with polar angle, and shear layers and boundary structures are present, so the decoupling condition is no longer equivalent in different propagation directions. The physically relevant decoupling depth for a given photon is the residual optical

depth along its own propagation direction,

$$\tau_{\text{out}}(\hat{\Omega}) = \int_{\text{ray}} n'_e \sigma_T ds', \quad ds' = \Gamma (1 - \beta \cdot \hat{\Omega}) ds. \quad (1)$$

This definition naturally incorporates non-radial structure and viewing-geometry effects: at the same location, different propagation directions may correspond to substantially different decoupling depths, thereby altering the last-scattering distribution and the efficiency of spectral broadening and polarization generation (Pe’er 2008; Beloborodov 2011; Lundman et al. 2014; Ito et al. 2013). Accordingly, in our Monte Carlo implementation we evaluate $\tau_{\text{out}}(\hat{\Omega})$ dynamically along each photon trajectory and use it consistently as the escape criterion, the coordinate defining dissipation windows, and the reference quantity for last-scattering statistics, ensuring an algorithmically unified treatment of geometric effects in structured jets.

3. SRHD BACKGROUND: EQUATIONS, NUMERICAL IMPLEMENTATION, AND DATA OUTPUT

We perform two-dimensional axisymmetric (r – z) special relativistic hydrodynamic (SRHD) simulations to generate the jet background, which serves as the external input for the subsequent Monte Carlo photospheric radiative transfer. In this section we summarise the governing equations, numerical scheme, and output strategy. Further implementation details (primitive-variable recovery, floor treatment, axis handling, etc.) are deferred to Appendix A.

3.1. *Governing equations and equation of state*

The SRHD equations are solved in flat Minkowski spacetime without magnetic fields, adopting units with $c = 1$. The primitive variables are $\{\rho, p, v_r, v_z\}$, where ρ is the comoving rest-mass density. The conserved variables are defined as

$$D = \rho W, \quad S_r = \rho h W^2 v_r, \quad S_z = \rho h W^2 v_z, \quad \tau = \rho h W^2 - p \quad (2)$$

where $W = (1 - v^2)^{-1/2}$ is the Lorentz factor and $v^2 = v_r^2 + v_z^2$. The specific enthalpy follows an ideal-gas (γ -law) equation of state,

$$h(\rho, p) = 1 + \frac{\gamma_{\text{ad}} p}{\gamma_{\text{ad}} - 1 \rho}, \quad \gamma_{\text{ad}} = 4/3, \quad (3)$$

which yields the sound speed

$$c_s^2 = \frac{\gamma_{\text{ad}} p}{\rho h}. \quad (4)$$

These expressions follow the standard conservative formulation of SRHD (Martí & Müller 1996, 1999; Toro 1999).

In axisymmetric cylindrical coordinates, the conservation equations can be written as

$$\partial_t \mathbf{U} + \partial_r \mathbf{F}_r(\mathbf{U}) + \partial_z \mathbf{F}_z(\mathbf{U}) = \mathbf{S}_{\text{axi}}, \quad (5)$$

where $\mathbf{U} = (D, S_r, S_z, \tau)^\top$. The geometric source terms associated with axisymmetry are treated explicitly; details of their implementation and numerical handling near the axis are given in Appendix A (Martí & Müller 1999).

3.2. Numerical scheme: finite volume, HLL flux, and RK2 time integration

Spatial discretisation is performed within a finite-volume Godunov framework. Intercell fluxes are computed using the HLL (Harten–Lax–van Leer) approximate Riemann solver (Harten et al. 1983; Toro 1999; LeVeque 2002):

$$\mathbf{F}_{\text{HLL}} = \begin{cases} \mathbf{F}(\mathbf{U}_L), & s_L \geq 0, \\ \mathbf{F}(\mathbf{U}_R), & s_R \leq 0, \\ \frac{s_R \mathbf{F}(\mathbf{U}_L) - s_L \mathbf{F}(\mathbf{U}_R) + s_L s_R (\mathbf{U}_R - \mathbf{U}_L)}{s_R - s_L}, & s_L < 0 < s_R, \end{cases} \quad \text{fp}_{\text{seff}} = [\text{median}(t_{k+1} - t_k)]^{-1}. \quad (6)$$

where s_L and s_R denote the minimum and maximum signal speeds estimated from the relativistic sound speed and normal velocities (see Appendix for details).

The timestep is determined by a Courant–Friedrichs–Lewy (CFL) condition,

$$\Delta t = \text{CFL} \min \left(\frac{\Delta r}{s_{\text{max},r}}, \frac{\Delta z}{s_{\text{max},z}} \right), \quad (7)$$

and time integration is performed using a second-order Runge–Kutta (Heun) scheme,

$$\mathbf{U}^{(1)} = \mathbf{U}^n + \Delta t \mathcal{R}(\mathbf{U}^n), \quad \mathbf{U}^{n+1} = \mathbf{U}^n + \frac{\Delta t}{2} \left[\mathcal{R}(\mathbf{U}^n) + \mathcal{R}(\mathbf{U}^{(1)}) \right], \quad (8)$$

where \mathcal{R} represents the combined flux divergence and geometric source terms. By default, piecewise-constant reconstruction is adopted, with an optional MUSCL–TVD extension to assess resolution dependence (van Leer 1979; Toro 1999).

3.3. Jet injection, boundary conditions, and ambient medium

Reflective boundary conditions are imposed at the symmetry axis ($r = 0$), while outflow conditions are used at the outer boundaries. The lower boundary serves as the jet injection region.

The jet is injected through a virtual nozzle geometry with injection radius

$$r_j = z_0 \tan \theta_j, \quad (9)$$

where the injection state is specified by (Γ_0, h_0) and the isotropic-equivalent luminosity L_{iso} . The inlet density and pressure normalisation are obtained from energy-flux scaling relations (see Appendix for details). Such setups are commonly adopted in SRHD simulations of GRB jets (Aloy et al. 2000; Zhang et al. 2003; Morsony et al. 2007). The ambient medium is modelled as a spherically symmetric power-law density profile.

3.4. Output snapshots and temporal sampling

The SRHD background is stored as a sequence of HDF5 (Hierarchical Data Format version 5) files. Each snapshot records $\{r_{\text{cent}}, z_{\text{cent}}\}$, the primitive variables ρ, p, v_r, v_z , and Γ , together with the corresponding physical time t_k .

Because the timestep varies adaptively according to the CFL condition, outputs written at fixed iteration intervals are not strictly equally spaced in time. We

therefore define an effective frame rate,

$$\text{fp}_{\text{seff}} = [\text{median}(t_{k+1} - t_k)]^{-1}. \quad (10)$$

3.5. Representative background structure: Lorentz factor, density, and pressure

Figures 2–4 show representative slices of the axisymmetric SRHD jet background at selected output times. The Monte Carlo radiative transfer primarily utilises snapshots within the interval `collapsar_srhds_step002000--003000.h5`, with the physical time t_k recorded in each file and used consistently in post-processing.

The jet core exhibits a high-Lorentz-factor region extending along the symmetry axis, with pronounced shear layers and strong gradients at the interface with the surrounding medium. The contrast in density and pressure between the jet and the ambient medium determines the spatial distribution of the electron number density and the effective scattering optical depth. These angular and transverse inhomogeneities directly influence the statistical distribution of last-scattering locations and the anisotropy of the radiation field in the subsequent transfer calculations (see Section 4).

4. MONTE CARLO IMPLEMENTATION

In this section, we describe the numerical implementation of the Monte Carlo Radiation Transfer (MCRT) method adopted in this work (Pozdnyakov et al. 1983; Chandrasekhar 1960; Rybicki & Lightman 1979). Unlike analytical treatments based on continuous radiation hydrodynamics (e.g., moment equations of the radiative transfer equation yielding luminosity evolution, jet acceleration, and pair-loading factor evolution

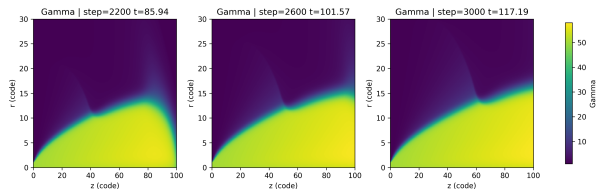


Figure 2. Lorentz factor distribution $\Gamma(r, z)$ of the two-dimensional axisymmetric SRHD jet background. The high- Γ jet core extends along the symmetry axis, with shear and boundary structures clearly visible at the interface with the surrounding medium. This structured flow field provides the dynamical background for the subsequent photospheric radiative transfer calculations.

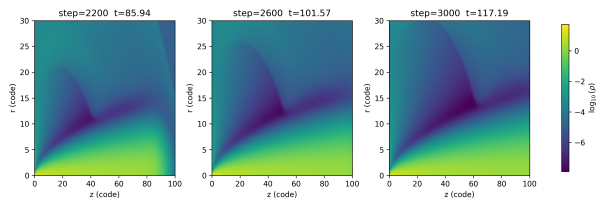


Figure 3. Density distribution at representative output times, shown as $\log_{10} \rho(r, z)$ to emphasise the strong contrast between the jet and the ambient medium. The density gradients and envelope structure determine the local electron number density and the effective scattering optical depth, thereby influencing the spatial distribution of photon decoupling.

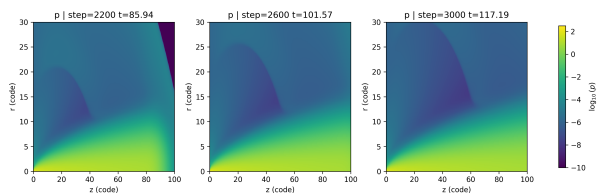


Figure 4. Pressure distribution at representative times, displayed as $\log_{10} p(r, z)$. The pressure structure reflects the internal thermal content of the jet and the confinement imposed by the ambient medium, and provides the background scaling for the parameterised heating prescriptions adopted in the radiative transfer calculations.

$Z_{\pm} = n_{\pm}/n_p$, demonstrating how sub-photospheric dissipation sustains optical depth and reshapes the peak energy E_{pk} ; see Beloborodov 2010; Vurm & Beloborodov 2016), our numerical approach follows individual photon packets in a prescribed background flow field, neglecting radiative feedback on the hydrodynamics (Santana et al. 2014; Ito et al. 2013; Parsotan & Lazzati 2023).

Analytical radiation–hydrodynamic models describe the coupled evolution of radiation and matter in an averaged sense through moment closure relations, typically valid under quasi-steady and near-spherical conditions. By contrast, the Monte Carlo approach explicitly tracks the scattering history of individual photons

in a given SRHD background, thereby avoiding angular closure assumptions and naturally incorporating strong anisotropy, structured jets, and polarization effects (Beloborodov 2011; Lundman et al. 2014).

The purpose of this section is to detail the statistical implementation of photon propagation, Klein–Nishina Compton scattering, polarization (Stokes vector) updates, and the post-processing procedure for observers characterized by viewing angle θ_{obs} and detector acceptance cone θ_{det} .

4.1. SRHD Background, Interpolation, and Electron Density

SRHD Background and Geometry.—Radiative transfer is performed on a two-dimensional axisymmetric SRHD background. Each hydrodynamic snapshot provides cell-centered quantities $\rho(R_{\text{cyl}}, z, t)$, $p(R_{\text{cyl}}, z, t)$, and $\mathbf{v}(R_{\text{cyl}}, z, t)$ (or equivalently Γ and β). Within each grid cell, the background is treated as piecewise constant. When a photon crosses a cell boundary, local quantities ρ , p , Γ , and β are updated accordingly (Santana et al. 2014; Ito et al. 2013).

For time-dependent simulations based on discrete snapshots $\{t_k\}$, the background at time $t \in [t_k, t_{k+1})$ is taken from snapshot k . Linear interpolation may alternatively be used to reduce temporal discretization error (Press et al. 1992); in this work we adopt the piecewise-constant scheme.

Electron Density and Pair Loading.—In SRHD, ρ denotes the comoving rest-mass density. The comoving proton number density is therefore

$$n'_p(R_{\text{cyl}}, z, t) = \frac{\rho(R_{\text{cyl}}, z, t)}{m_p}. \quad (11)$$

If pair production is included, the total comoving electron number density becomes

$$n'_e(R_{\text{cyl}}, z, t) = (1 + Z_{\pm}) \frac{\rho(R_{\text{cyl}}, z, t)}{m_p}, \quad (12)$$

where Z_{\pm} may be treated as a constant parameter or supplied by a semi-analytical model. In this work, Z_{\pm} is treated as a controllable parameter to investigate its impact on the photospheric radius, spectral shape, and polarization.

4.2. Injection Conditions: Injection Surface, Initial Photons, and Stokes Parameters

Injection Surface.—Photons are injected in regions of high optical depth where the radiation field is approximately thermal (Pe'er 2008; Beloborodov 2011). In the SRHD background, the injection surface is defined geometrically (e.g., a plane at $z = z_{\text{init}}$ within $R_{\text{cyl}} \leq R_{\text{inj}}$).

The outward optical depth τ_{out} is computed dynamically to ensure $\tau_{\text{out}} \gg 1$, guaranteeing injection in an optically thick region.

Initial Energy, Direction, and Stokes Vector.—Photon energies are sampled in the local comoving frame from a blackbody (or quasi-thermal) distribution (Rybicki & Lightman 1979):

$$p(E'_\gamma) \propto \frac{E'^2_\gamma}{\exp(E'_\gamma/kT'_\gamma) - 1}. \quad (13)$$

Initial directions are isotropic in the comoving frame. Photons are initialized as unpolarized with Stokes vector

$$\mathbf{S} = (I, Q, U)^\top, \quad Q = U = 0, \quad (14)$$

neglecting circular polarization. Each photon packet carries a statistical weight w .

4.3. Optical Depth Sampling and Dynamic Determination of Interaction Sites

For each scattering event, the cumulative optical depth is sampled from

$$\Delta\tau = -\ln \xi, \quad \xi \in (0, 1), \quad (15)$$

corresponding to the exponential free-path distribution in optical depth space (Pozdnyakov et al. 1983).

Photon propagation proceeds via ray-marching in the laboratory frame. Within each grid cell, local quantities are treated as constant and the optical depth increment is

$$d\tau = n'_e \sigma_T ds', \quad ds' = \Gamma(1 - \beta \cdot \hat{\Omega}) ds, \quad (16)$$

where ds is the lab-frame path length and ds' is the corresponding comoving interval (Rybicki & Lightman 1979).

4.4. Escape Criterion

After each scattering, the remaining optical depth along the outgoing direction is computed as

$$\tau_{\text{out}}(\hat{\Omega}_{\text{out}}) = \int_{\text{ray}} n'_e \sigma_T ds'. \quad (17)$$

If $\tau_{\text{out}} < \tau_{\text{esc}}$ (with $\tau_{\text{esc}} \sim 1$), the photon is considered decoupled and recorded (Pe'er 2008; Beloborodov 2011; Lundman et al. 2014; Ito et al. 2013); otherwise, the next scattering cycle is initiated.

4.5. Adiabatic Cooling Between Scatterings

Between scatterings, photons experience adiabatic cooling in the expanding outflow. We adopt the effective scaling

$$E'_\gamma \propto r^{-2/3}, \quad (18)$$

implemented numerically as

$$E'_{\gamma,\text{new}} = E'_{\gamma,\text{old}} \left(\frac{r_{\text{new}}}{r_{\text{old}}} \right)^{-2/3}, \quad (19)$$

following common practice in photospheric post-processing treatments (Beloborodov 2011; Ito et al. 2013).

4.6. Electron Sampling and Scattering in the Electron Rest Frame

At each interaction, electron velocities are sampled from a Maxwell–Jüttner distribution in the comoving frame (Jüttner 1911):

$$f(\gamma_e) d\gamma_e \propto \gamma_e^2 \beta_e \exp\left(-\frac{\gamma_e}{\Theta_e}\right) d\gamma_e, \quad \Theta_e = \frac{kT'_e}{m_e c^2}. \quad (20)$$

The scattering is performed in the electron rest frame (ERF) and transformed back to the comoving and laboratory frames.

4.7. Klein–Nishina Sampling and Polarization Update

In the ERF, the scattered photon energy satisfies

$$\varepsilon_f = \frac{\varepsilon_i}{1 + \varepsilon_i(1 - \cos\theta_{\text{sc}})}, \quad (21)$$

where $\varepsilon_i = E_i/(m_e c^2)$. Scattering angles are sampled from the Klein–Nishina differential cross section using rejection sampling (Klein & Nishina 1929; Pozdnyakov et al. 1983).

Polarization evolution is treated using Stokes vectors. After rotating into the scattering-plane basis, the Stokes vector is updated via the Mueller matrix:

$$\mathbf{S}_{\text{out}} = \mathbf{R}(-\psi) \mathbf{M}_{\text{KN}}(\varepsilon_i, \theta_{\text{sc}}) \mathbf{R}(\psi) \mathbf{S}_{\text{in}}. \quad (22)$$

4.8. Sub-photospheric Reheating

To model sub-photospheric energy dissipation and unsaturated Comptonization, we introduce parameterized reheating (Beloborodov 2010; Vurm & Beloborodov 2016). If a scattering event occurs within

$$\tau_{\text{diss,min}} \leq \tau_{\text{out}} \leq \tau_{\text{diss,max}}, \quad (23)$$

and the scattering count satisfies $n_{\text{scat}} \bmod n_{\text{rh}} = 0$, the electron temperature is incremented to maintain $y \sim \mathcal{O}(1)$.

4.9. Observer Post-processing

Arrival Time and Energy.—The observed arrival time is computed using equal-arrival-time geometry

$$t_{\text{obs}} = \frac{1}{1+z} \left(t - \frac{\hat{\mathbf{k}} \cdot \mathbf{r}}{c} \right), \quad (24)$$

(Granot et al. 1999), with observed energy $E_{\text{obs}} = E/(1+z)$.

Time-resolved Spectra.—Within each time bin, spectra are constructed and fitted with the Band function (Band et al. 1993) to obtain $(\alpha, \beta, E_{\text{pk}})$.

Polarization.—Stokes parameters are summed within bins:

$$I_{\text{bin}} = \sum_i w_i, \quad Q_{\text{bin}} = \sum_i w_i q_i, \quad U_{\text{bin}} = \sum_i w_i u_i, \quad (25)$$

yielding polarization degree and angle:

$$\Pi = \frac{\sqrt{Q_{\text{bin}}^2 + U_{\text{bin}}^2}}{I_{\text{bin}}}, \quad \chi = \frac{1}{2} \arctan\left(\frac{U_{\text{bin}}}{Q_{\text{bin}}}\right). \quad (26)$$

This definition follows the standard post-processing procedure for scattering-induced polarization (Chandrasekhar 1960; Lundman et al. 2014).

5. RESULTS

In this section we present the Monte Carlo radiative transfer results obtained on top of the time-dependent SRHD jet background described in Section 3 and Section 4. Unless stated otherwise, photon escape is determined using the residual optical depth evaluated along the instantaneous photon propagation direction, $\tau_{\text{out}}(\hat{\Omega})$. The SRHD background is treated as piecewise constant in time. Unless otherwise stated, each time bin contains at least ~ 200 escaping photons.

5.1. Baseline model: no dissipation and no pair loading

We begin with a baseline model in which no subphotospheric dissipation is included and the pair loading parameter is set to $Z_{\pm} = 0$. Photons are injected at large optical depths with a comoving quasi-thermal distribution, and subsequently decouple gradually through multiple Compton scatterings off thermal electrons and geometric expansion. No additional energy injection or non-thermal particle acceleration is introduced.

Figure 5 compares the time-resolved radiation properties for two different injection depths ($z = 64$ and $z = 74$). The top panels show the normalized light curve (black line) together with the time-resolved peak energy $E_{\text{pk}}(t)$ (symbols; right axis). The bottom panels show the spectral width,

$$W(t) = \log_{10}(E_{90}/E_{10}), \quad (27)$$

where E_{10} and E_{90} enclose 10% and 90% of the cumulative νF_{ν} distribution, respectively.

For both injection depths, the light curve exhibits a single-peaked, nearly symmetric pulse with smooth rise and decay phases, indicating that the temporal structure is primarily regulated by the geometric expansion of the

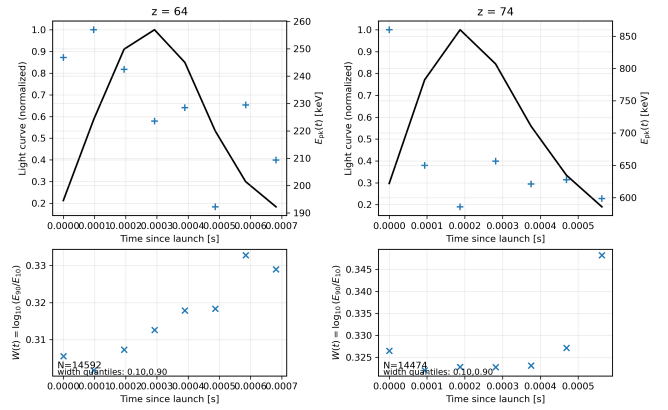


Figure 5. Baseline model comparison between two injection depths. Left and right columns correspond to $z = 64$ and $z = 74$, respectively. Top panels: normalized light curve (black line) and time-resolved peak energy $E_{\text{pk}}(t)$ (symbols; right axis). Bottom panels: spectral width $W(t) = \log_{10}(E_{90}/E_{10})$, where E_{10} and E_{90} enclose 10% and 90% of the cumulative νF_{ν} distribution. In the absence of subphotospheric dissipation and pair loading, both the pulse morphology and the spectral-width evolution are highly consistent across injection depths, indicating a weak dependence on the initial optical depth.

outflow and the gradual decline of the optical depth. The peak energy $E_{\text{pk}}(t)$ varies only moderately during the pulse and does not show a strictly flux-tracking hard-to-soft (or soft-to-hard) evolution, suggesting that in the absence of subphotospheric dissipation the spectral peak is largely set by the injection conditions and adiabatic expansion.

The spectral width remains narrow throughout the pulse, with typical values $W \simeq 0.30$ – 0.35 and only weak temporal variations. This range is characteristic of quasi-thermal photospheric emission and is significantly narrower than the widths typically inferred for observed GRB Band spectra. Therefore, in the baseline model without dissipation and pair production, multiple scatterings and expansion smooth the spectrum but do not drive it far from a thermal-like shape.

Despite the different initial optical depths and decoupling radii implied by $z = 64$ and $z = 74$, the light-curve morphology, the range of $E_{\text{pk}}(t)$ evolution, and the distribution of $W(t)$ are highly consistent between the two cases. This indicates that, in the baseline setup, the radiation properties depend only weakly on the injection depth (or equivalently the initial optical depth), providing a robust reference for the comparisons below.

5.2. Subphotospheric dissipation: scanning the optical-depth window

To investigate how subphotospheric energy dissipation shapes the photospheric spectrum, we introduce a

parameterized reheating prescription that operates only within a finite optical-depth window, $\tau_{\text{diss,min}} \leq \tau_{\text{out}} \leq \tau_{\text{diss,max}}$. Within this window, the electron temperature is periodically boosted in a subset of scattering events, maintaining a non-zero Compton y -parameter.

Figure 6 summarizes the two-dimensional scan over $(\tau_{\text{diss,min}}, \tau_{\text{diss,max}})$. We present the changes in the peak energy E_{pk} , the low-energy spectral index α_{eff} , and the high-energy tail strength relative to the reference dissipation model $(\tau_{\text{diss,min}}, \tau_{\text{diss,max}}) = (3, 30)$.

The results show that the spectral response is highly sensitive to where dissipation occurs in optical depth, and the parameter space separates into distinct regimes. When dissipation occurs at shallow depths ($\tau_{\text{diss,min}} \simeq 1$), the peak energy increases significantly relative to the no-dissipation case, reaching $E_{\text{pk}}/E_{\text{pk},0} \sim 1.4$ – 1.7 . In this regime, energy injection happens before substantial adiabatic cooling, raising the mean photon energy. Meanwhile, α_{eff} decreases markedly, indicating that non-saturated Comptonization becomes increasingly important below the spectral peak and reshapes the low-energy spectrum.

In contrast, when dissipation is confined to deeper regions ($\tau_{\text{diss,min}} \gtrsim 10$), the peak energy is systematically reduced to $E_{\text{pk}}/E_{\text{pk},0} \sim 0.5$ – 0.6 . In this case photons undergo many additional scatterings after reheating before escaping, experiencing stronger thermalization and adiabatic cooling. The high-energy tail is correspondingly weaker and the spectrum approaches a quasi-thermal shape.

Between these extremes, an intermediate optical-depth window (typically $\tau_{\text{diss,min}} \sim 3$ and $\tau_{\text{diss,max}} \sim 20$ – 50) yields the most efficient non-saturated Comptonization. In this regime, E_{pk} remains close to the baseline value while the high-energy tail is maximized and α_{eff} changes only moderately, implying substantial spectral broadening without full thermalization.

Overall, these results demonstrate that the photospheric spectral shape is controlled not only by the dissipation strength, but crucially by the optical-depth range over which dissipation operates. Consequently, the observed E_{pk} , low-energy slope, and high-energy tail strength provide direct diagnostics of the dissipation depth in the subphotospheric region.

5.3. Effects of pair loading

We vary the electron–positron pair loading parameter Z_{\pm} while keeping all other conditions fixed, and quantify its impact on the time-integrated spectral properties and polarization. Figure 7 summarizes key observables relative to the no-pair case.

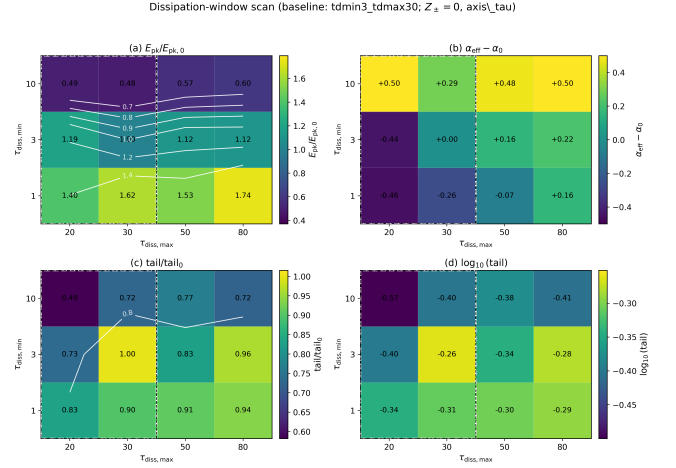


Figure 6. Two-dimensional phase space for the optical-depth window scan of subphotospheric dissipation. From left to right and top to bottom, panels show: relative change in peak energy $E_{\text{pk}}/E_{\text{pk},0}$, change in low-energy spectral index $\alpha_{\text{eff}} - \alpha_0$, relative high-energy tail strength $\text{tail}/\text{tail}_0$, and $\log_{10}(\text{tail})$, as functions of $(\tau_{\text{diss,min}}, \tau_{\text{diss,max}})$. All quantities are normalized to the reference dissipation model $(\tau_{\text{diss,min}}, \tau_{\text{diss,max}}) = (3, 30)$, marked by the dashed lines. Contours highlight systematic trends across parameter space.

First, the peak energy E_{pk} increases overall with Z_{\pm} . Although a mild non-monotonic behavior appears near $Z_{\pm} \sim 1$, the high pair-loading case ($Z_{\pm} = 3$) reaches $E_{\text{pk}} \simeq 1.25 E_{\text{pk},0}$. This trend suggests that pair loading strengthens the coupling between radiation and the plasma and prolongs energy exchange, delaying decoupling and thus increasing the observed peak energy.

Polarization responds more strongly and in the opposite sense: the time-integrated polarization degree increases markedly with Z_{\pm} , peaking around $Z_{\pm} \sim 1$ – 2 with $\Pi/\Pi_0 \simeq 1.4$ – 1.45 , and then decreases slightly at higher Z_{\pm} while remaining above the no-pair level. This indicates that additional pairs do not simply isotropize the radiation field; instead, within a certain range they can reshape the geometry and angular distribution of the last-scattering surface, enhancing the net polarization.

The high-energy tail strength decreases overall as Z_{\pm} increases, but the trend is not strictly monotonic. Compared to $Z_{\pm} = 0$, the tail is strongly suppressed at $Z_{\pm} \approx 0.3$, partially recovers near $Z_{\pm} = 1$, and is again suppressed for $Z_{\pm} \gtrsim 2$. This behavior reflects the sensitivity of high-energy photon production and escape to both the scattering depth and the time-dependent outflow history.

The low-energy spectral index shows the clearest systematic evolution: α_{eff} decreases monotonically with Z_{\pm} , reaching $\alpha - \alpha_0 \simeq -0.55$ at $Z_{\pm} = 3$. This cor-

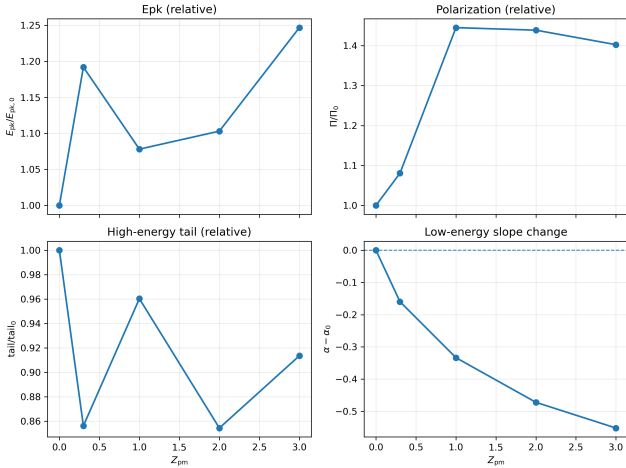


Figure 7. Relative changes in time-integrated quantities as functions of pair loading Z_{\pm} : $E_{pk}/E_{pk,0}$, Π/Π_0 , high-energy tail strength, and the change in low-energy spectral index.

responds to a progressively steeper sub-peak spectrum and can be attributed to the increased effective number of scatterings in the presence of additional pairs, which drives the low-energy photons closer to thermal equilibrium in the comoving frame.

In summary, pair loading modulates the effective scattering depth and decoupling history, systematically affecting the peak energy, the sub-peak spectral slope, and the high-energy tail, while also producing a pronounced impact on polarization. The correlated enhancement of Π and E_{pk} with increasing Z_{\pm} highlights the diagnostic power of polarization for constraining pair content and photospheric dynamics.

5.4. Viewing-angle dependence

Because the SRHD jet exhibits strong angular structure and velocity shear, the observed radiation properties depend systematically on the viewing angle θ_{obs} . This dependence mainly arises from two effects: (i) the reduction of the Doppler factor with increasing θ_{obs} , which causes de-boosting and arrival-time delays; and (ii) the increasing geometric asymmetry of the last-scattering surface off-axis, which enhances radiation anisotropy and alters spectral evolution. We therefore perform synthetic observations from on-axis to off-axis viewing angles and analyze the time-resolved light curves and spectral diagnostics.

Figure 8 shows the results for $\theta_{obs} = 0^\circ, 0.5^\circ, 1^\circ$, and 2° . The top panels present the normalized light curves (black) and $E_{pk}(t)$ (blue symbols; right axis). As the viewing angle moves off-axis, the pulse broadens and the peak time shifts systematically later. This behavior is consistent with a reduced Doppler factor and

the geometric broadening of equal-arrival-time surfaces (EATS).

At the current photon statistics, $E_{pk}(t)$ exhibits substantial scatter within individual time bins, making it difficult to infer a strictly monotonic temporal evolution for each viewing angle. Nevertheless, comparison across angles indicates that the characteristic time-integrated E_{pk} decreases with increasing θ_{obs} , consistent with Doppler de-boosting and the weighted contribution from larger-angle emission.

The bottom panels show the effective low-energy index $\alpha_{eff}(t)$. For on-axis and mildly off-axis views (0° and 0.5°), α_{eff} remains positive for most of the pulse and varies relatively smoothly. At larger viewing angles, the temporal scatter increases and $\alpha_{eff}(t)$ can become negative in some intervals. However, within the present statistical precision, α_{eff} does not exhibit a strictly monotonic dependence on θ_{obs} ; instead, off-axis viewing primarily enhances the time-dependent structure and variability of the sub-peak spectral shape.

We emphasize that the number of escaped photons within the acceptance cone decreases with viewing angle, amplifying statistical fluctuations in time-resolved spectral parameters. Therefore, interpretations of instantaneous indices in off-axis cases must account for both statistical uncertainty and genuine physical evolution.

Overall, increasing θ_{obs} broadens the pulse and delays the peak time, reduces the characteristic E_{pk} , and enhances the amplitude and scatter of the time evolution of the low-energy spectral shape.

5.5. Decoupling location distribution

To better understand the physical origin of the photospheric spectrum and polarization, we analyze the locations of the last scattering events, i.e., where photons undergo their final interaction with the plasma before escape. In the Monte Carlo calculation, each escaped photon records its last-scattering radius r_{last} , statistical weight, and Stokes parameters, enabling weighted statistics of the spatial structure of the decoupling region.

Figure 9a shows the weighted probability density distribution of r_{last} for all escaped photons. The last-scattering radii are not confined to a narrow geometric shell; instead, they span a finite but clearly broadened range of ~ 0.3 dex. The weighted median and the 16%–84% percentiles are $\log_{10}(r_{last}/\text{cm}) \simeq 10.16^{+0.11}_{-0.25}$, demonstrating that decoupling occurs over an extended region rather than an idealized thin photospheric surface. This reflects the statistical nature of photon decoupling in a time-dependent flow, where the last-scattering

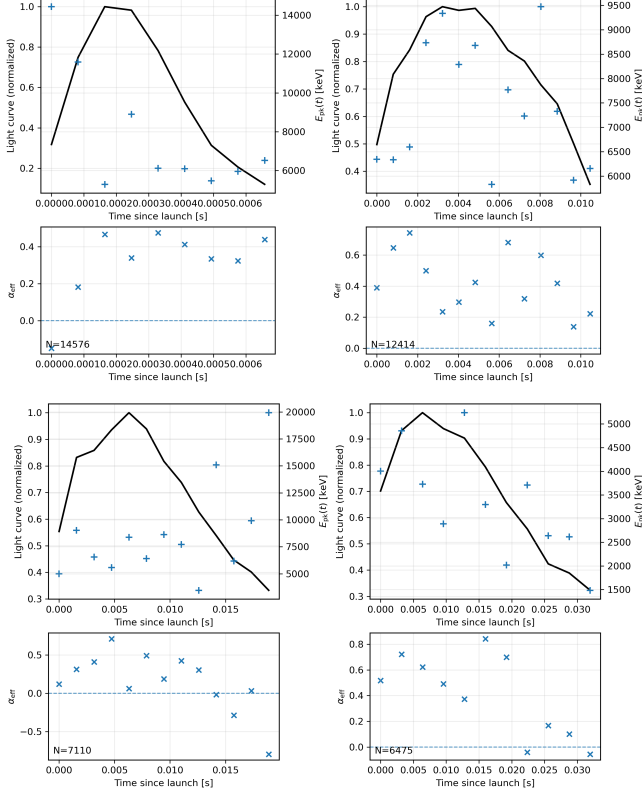


Figure 8. Viewing-angle dependence of time-resolved radiation properties. Top panel: on-axis and mildly off-axis views (0° , 0.5°). Bottom panel: off-axis views (1° , 2°). The panels show the normalized light curves, the time-resolved peak energy $E_{\text{pk}}(t)$, and the effective low-energy spectral index $\alpha_{\text{eff}}(t)$ for different viewing angles (see text for definitions).

location is shaped by both local dynamics and the radiative transfer history.

Figure 9b shows the weighted median r_{last} as a function of observed energy E_{obs} using equal-weight energy grouping. The variation of $\log_{10}(r_{\text{last}})$ with energy is limited and does not show a clear monotonic trend. At the current statistics, differences among energy groups are typically at the $\sim 10^{-2}$ dex level ($\lesssim 0.015$ dex). The inset shows that the median scattering number n_{scat} varies similarly weakly across energy groups, implying that the mild energy dependence is unlikely to be driven by large differences in scattering counts, and may instead be related to the spatiotemporal structure of the extended decoupling region.

Figure 9c shows the polarization degree $\Pi(r_{\text{last}})$ as a function of decoupling radius. The polarization degree is computed by weighted summation of Stokes parameters within each radius bin, and uncertainties are estimated via bootstrap resampling. We find clear structural variations of Π across the decoupling region, with typical values of a few percent and reaching $\sim 7\%$ in some in-

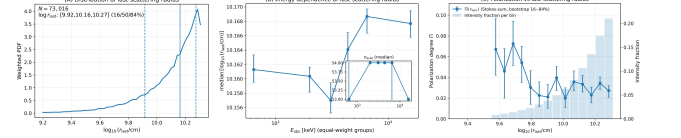


Figure 9. Statistical properties of photon decoupling locations. (a) Weighted probability density of the last-scattering radius r_{last} ; vertical lines mark the weighted 16%, 50%, and 84% percentiles, showing that decoupling occurs over an extended radial range rather than a thin shell. (b) Weighted median r_{last} as a function of observed energy E_{obs} using equal-weight energy bins; error bars show the bootstrap 16%–84% intervals. The inset shows the corresponding median scattering number n_{scat} . (c) Polarization degree Π as a function of r_{last} ; error bars are bootstrap 16%–84% intervals, and the grey histogram indicates the relative intensity contribution from each radius bin.

tervals. Notably, the radius range contributing most strongly to the total intensity (grey histogram) does not coincide with extreme polarization peaks, indicating that the observed net polarization is an aggregate of contributions from multiple radii rather than being dominated by a single shell.

In summary, in a time-dependent structured outflow the decoupling region is spatially extended; its energy dependence is mild and non-monotonic; and the net polarization arises from a weighted superposition over an extended last-scattering region, rather than a single photospheric radius.

6. DISCUSSION AND CONCLUSIONS

We have investigated the time-resolved spectral diagnostics and polarization properties of photospheric emission from a structured jet by performing Monte Carlo radiative transfer on top of a two-dimensional, axisymmetric, time-dependent SRHD outflow. Photon escape is determined using the residual optical depth along the instantaneous photon direction, $\tau_{\text{out}}(\hat{\Omega})$, and the SRHD background is treated as piecewise constant in time, enabling a consistent tracking of photon decoupling and spectral formation in both geometry and time.

Our main findings are summarized as follows:

- *Baseline model (no dissipation, no pair loading):* The emission produces a single-peaked, nearly symmetric pulse, and $E_{\text{pk}}(t)$ shows only moderate evolution without strict flux-tracking hard-to-soft behavior. The spectral width $W = \log_{10}(E_{90}/E_{10})$ remains narrow throughout the pulse ($W \sim 0.30$ – 0.35), consistent with quasi-thermal photospheric emission. Results from different injection depths (e.g. $z = 64$ and $z = 74$) are highly consistent in pulse morphology, $E_{\text{pk}}(t)$

evolution, and $W(t)$ distribution, indicating a weak sensitivity to the initial optical depth and providing a robust reference baseline.

- *Optical-depth window of subphotospheric dissipation:* The spectral outcome is strongly sensitive to the dissipation depth and exhibits distinct regimes. Shallow dissipation increases E_{pk} and drives the spectrum toward a broader non-thermal shape, whereas deep dissipation tends to re-thermalize the spectrum, lowering E_{pk} and suppressing the high-energy tail. Intermediate optical-depth windows maximize non-saturated Comptonization, producing the strongest high-energy tails while keeping E_{pk} close to the baseline value. These trends imply that E_{pk} , the sub-peak spectral slope, and the tail strength can be used to diagnose the dissipation depth.
- *Pair loading:* Increasing Z_{\pm} generally increases E_{pk} and steepens the sub-peak spectrum, while the high-energy tail is suppressed overall but can vary non-monotonically. The time-integrated polarization degree responds strongly to Z_{\pm} , peaking at intermediate pair loading and remaining enhanced relative to the no-pair case. This highlights the diagnostic potential of polarization for constraining pair content and photospheric dynamics.
- *Viewing-angle dependence:* As θ_{obs} increases, the pulse broadens and the peak time is delayed, consistent with Doppler de-boosting and EATS broadening. The characteristic time-integrated E_{pk} decreases with viewing angle, while time-resolved spectral parameters exhibit larger scatter off-axis due to both geometric mixing and reduced photon statistics.

- *Extended decoupling region and polarization origin:* The last-scattering radius distribution demonstrates that decoupling occurs over an extended radial range rather than a thin photospheric surface. Energy dependence of r_{last} is mild ($\sim 10^{-2}$ dex) and non-monotonic. The polarization degree varies structurally with r_{last} , and the observed net polarization is produced by weighted contributions from multiple radii, linking polarization to the geometry and anisotropy of the extended decoupling region.

The main limitations of this work include the parameterized treatment of subphotospheric dissipation and pair production, the neglect of magnetic-field-related radiation processes, and the omission of radiative feedback on the hydrodynamic evolution. Future developments toward self-consistent radiation (magneto-)hydrodynamic simulations incorporating energy injection, pair creation, and radiative feedback will be essential for further testing structured-jet photospheric models for GRB prompt emission and for improving the reliability of joint inference of jet structure and dissipation location using spectral and polarization diagnostics.

ACKNOWLEDGEMENTS

We thank Dr. Qingwen Tang for helpful guidance and continuous support during the development of this work. We are also grateful to friends and colleagues for valuable discussions and encouragement.

This work made use of the computational resources provided by the LHAASO (Large High Altitude Air Shower Observatory) computing platform. We acknowledge the support of the LHAASO high-performance computing facilities used for the numerical simulations in this study.

REFERENCES

- Band, D., Matteson, J., Ford, L., et al. 1993, BATSE observations of gamma-ray burst spectra. I. Spectral diversity, *ApJ*, 413, 281
- Kaneko, Y., et al. 2006, The Complete Spectral Catalog of Bright BATSE Gamma-Ray Bursts, *ApJS*, 166, 298
- Axelsson, M., & Borgonovo, L. 2015, The width of gamma-ray burst spectra, *MNRAS*, 447, 3150
- Piran, T. 2004, The physics of gamma-ray bursts, *Rev. Mod. Phys.*, 76, 1143
- Mészáros, P. 2006, Gamma-ray bursts, *Rep. Prog. Phys.*, 69, 2259
- Kole, M., et al. 2020, Prompt Emission Polarimetry of Gamma-Ray Bursts with the AstroSat CZT Imager, *A&A*, 644, A124
- Chattopadhyay, T., et al. 2019, Prompt Emission Polarimetry of Gamma-Ray Bursts with the AstroSat CZT Imager, *ApJ*, 884, 123
- Chattopadhyay, T., et al. 2022, Hard X-ray polarization catalog for a five-year sample of Gamma-Ray Bursts using AstroSat CZT-Imager, *MNRAS*, 509, 2758
- Paczynski, B. 1986, Gamma-ray bursters at cosmological distances, *ApJ*, 308, L43
- Goodman, J. 1986, Are gamma-ray bursts optically thick?, *ApJ*, 308, L47

- Pe'er, A. 2008, Temporal evolution of thermal emission from relativistically expanding plasma, *ApJ*, 682, 463
- Beloborodov, A. M. 2011, Radiative transfer in ultrarelativistic outflows, *ApJ*, 737, 68
- Lundman, C., Pe'er, A., & Ryde, F. 2013, A theory of photospheric emission from relativistic, collimated outflows, *MNRAS*, 428, 2430
- Lundman, C., Pe'er, A., & Ryde, F. 2014, Polarization properties of photospheric emission from relativistic, collimated outflows, *MNRAS*, 440, 3292
- Beloborodov, A. M. 2010, Collisional mechanism for gamma-ray burst emission, *MNRAS*, 407, 1033
- Vurm, I., & Beloborodov, A. M. 2016, Radiative transfer models for gamma-ray bursts, *ApJ*, 831, 175
- Giannios, D. 2006, Prompt emission spectra from the photosphere of a GRB, *A&A*, 457, 763
- Beloborodov, A. M. 2017, Sub-photospheric shocks in relativistic explosions, *ApJ*, 838, 125
- Ito, H., Nagataki, S., Matsumoto, J., Lee, S.-H., & De Colle, F. 2013, Photospheric emission from stratified jets, *ApJ*, 777, 62
- Santana, R., Barniol Duran, R., & Kumar, P. 2014, Magnetic fields in relativistic collisionless shocks, *ApJ*, 785, 29
- Parsotan, T. M., & Lazzati, D. 2023, Monte Carlo simulations of photospheric emission in gamma-ray bursts, in *Proc. of the 16th Marcel Grossmann Meeting on General Relativity, Astrophysics and Cosmology, 2972–2981*, World Scientific
- Rees, M. J., & Mészáros, P. 1994, Unsteady outflow models for cosmological gamma-ray bursts, *ApJ*, 430, L93
- Thompson, C. 1994, A model of gamma-ray bursts, *MNRAS*, 270, 480
- Mészáros, P., & Rees, M. J. 2000, Steep slopes and preferred breaks in GRB spectra: the role of photospheres and Comptonization, *ApJ*, 530, 292
- Levinson, A., & Nakar, E. 2020, Physics of radiation mediated shocks and its applications to GRBs, supernovae, and neutron star mergers, *Phys. Rep.*, 866, 1–46
- Harten, A., Lax, P. D., & van Leer, B. 1983, On upstream differencing and Godunov-type schemes for hyperbolic conservation laws, *SIAM Rev.*, 25, 35
- Toro, E. F. 1999, *Riemann Solvers and Numerical Methods for Fluid Dynamics: A Practical Introduction*, 2nd edn., Springer
- LeVeque, R. J. 2002, *Finite Volume Methods for Hyperbolic Problems*, Cambridge University Press
- van Leer, B. 1979, Towards the ultimate conservative difference scheme. V. A second-order sequel to Godunov's method, *J. Comput. Phys.*, 32, 101
- Martí, J. M., & Müller, E. 1996, Numerical hydrodynamics in special relativity, *J. Comput. Phys.*, 123, 1
- Martí, J. M., & Müller, E. 1999, Numerical Hydrodynamics in Special Relativity, *Living Rev. Relativ.*, 2, 3
- Chandrasekhar, S. 1960, *Radiative Transfer*, Dover
- Rybicki, G. B., & Lightman, A. P. 1979, *Radiative Processes in Astrophysics*, Wiley
- Mihalas, D., & Mihalas, B. W. 1984, *Foundations of Radiation Hydrodynamics*, Oxford Univ. Press
- Pozdnyakov, L. A., Sobol, I. M., & Sunyaev, R. A. 1983, Comptonization and the shaping of X-ray source spectra – Monte Carlo calculations, *Astrophys. Space Phys. Rev.*, 2, 189–331
- Press, W. H., Teukolsky, S. A., Vetterling, W. T., & Flannery, B. P. 1992, *Numerical Recipes in C: The Art of Scientific Computing*, 2nd edn., Cambridge University Press
- Klein, O., & Nishina, Y. 1929, Über die Streuung von Strahlung durch freie Elektronen nach der neuen relativistischen Quantendynamik von Dirac, *Z. Phys.*, 52, 853–868
- Jüttner, F. 1911, Das Maxwellsche Gesetz der Geschwindigkeitsverteilung in der Relativtheorie, *Ann. Phys.*, 339, 856–882
- Aloy, M. A., Müller, E., Ibáñez, J. M., Martí, J. M., & MacFadyen, A. 2000, Relativistic jets from collapsars, *ApJL*, 531, L119
- Zhang, W., Woosley, S. E., & MacFadyen, A. I. 2003, Relativistic jets in collapsars, *ApJ*, 586, 356
- Morsony, B. J., Lazzati, D., & Begelman, M. C. 2007, Temporal and angular properties of gamma-ray burst jets emerging from massive stars, *ApJ*, 665, 569
- Compton, A. H. 1923, A quantum theory of the scattering of X-rays by light elements, *Phys. Rev.*, 21, 483–502
- Granot, J., Piran, T., & Sari, R. 1999, Images and spectra from the interior of a relativistic fireball, *ApJ*, 513, 679–689

APPENDIX

A. NUMERICAL IMPLEMENTATION DETAILS OF THE SRHD SOLVER

This appendix summarizes numerical implementation details of the SRHD background used in this work, including the treatment of axisymmetric geometric source terms, the explicit expressions for the characteristic wave-speed bounds, the primitive-variable recovery procedure, and the floors/ceilings applied for robustness. Our implementation follows standard practices in relativistic hydrodynamics (Martí & Müller 1996, 1999; Toro 1999; LeVeque 2002), with choices tuned to prioritize smoothness and robustness of the background flow for subsequent radiative-transfer post-processing.

A.1. Axisymmetric geometric source terms and near-axis treatment

In axisymmetric cylindrical coordinates (r, z) , the SRHD equations in conservative form can be written as

$$\partial_t \mathbf{U} + \partial_r \mathbf{F}_r + \partial_z \mathbf{F}_z = \mathbf{S}_{\text{axi}}, \quad (\text{A1})$$

where $\mathbf{U} = (D, S_r, S_z, \tau)^\top$. In an ideal formulation, the radial flux divergence would be discretized as $\frac{1}{r} \partial_r (r \mathbf{F}_r)$. However, this form can introduce numerical instability as $r \rightarrow 0$.

To improve robustness, we adopt the common strategy of using a ‘‘Cartesian-like’’ flux divergence supplemented by an explicit geometric source term. Specifically, we include the axisymmetric source term only in the radial momentum equation,

$$S_{\text{axi}, S_r} = \frac{p}{r}, \quad (\text{A2})$$

and in practice enforce a lower bound on r ,

$$r \rightarrow \max(r, r_{\text{floor}}), \quad r_{\text{floor}} = 10^{-12}, \quad (\text{A3})$$

to avoid division by zero. This treatment preserves the overall conservative structure while substantially reducing numerical noise near the symmetry axis, and is widely used in SRHD jet simulations (Martí & Müller 1999; Aloy et al. 2000).

A.2. Characteristic wave-speed bounds

The HLL flux requires estimates of the left and right signal-speed bounds, s_L and s_R . These are obtained from the relativistic sound speed and the normal velocity. For an interface with normal direction $\hat{\mathbf{n}}$, define the normal velocity $v_n = \mathbf{v} \cdot \hat{\mathbf{n}}$. The characteristic speeds are then approximated by

$$\lambda_{\pm} = \frac{v_n \pm c_s}{1 \pm v_n c_s}, \quad (\text{A4})$$

where the relativistic sound speed c_s is given by Eq. (4). After computing $\lambda_{\pm}^{(L)}$ and $\lambda_{\pm}^{(R)}$ on the left and right states, we set

$$s_L = \min\left(0, \lambda_-^{(L)}, \lambda_-^{(R)}\right), \quad s_R = \max\left(0, \lambda_+^{(L)}, \lambda_+^{(R)}\right), \quad (\text{A5})$$

as the wave-speed bounds for the HLL solver. This choice is known to be stable and broadly applicable in relativistic hydrodynamics (Toro 1999; Martí & Müller 1996).

A.3. Primitive-variable recovery: pressure bracketing and bisection

Recovering primitive variables (ρ, p, \mathbf{v}) from the conserved state \mathbf{U} can be particularly sensitive in the presence of high Lorentz factors and strong shocks. We adopt a cell-wise ‘‘pressure bracketing + bisection’’ strategy (Martí & Müller 1999).

Concretely, the recovery is reduced to solving a one-dimensional nonlinear root-finding problem for the pressure p . We perform a bisection search within a bracket $[p_{\min}, p_{\max}]$, where

$$p_{\min} = p_{\text{floor}}, \quad p_{\max} = \max(p_{\text{guess}}, p_{\text{floor}}), \quad (\text{A6})$$

and p_{guess} is estimated either from the previous time step or from a local equilibrium-based approximation. We declare convergence when the relative change satisfies

$$\left| \frac{p^{(k+1)} - p^{(k)}}{p^{(k)}} \right| < \epsilon_{\text{tol}}, \quad \epsilon_{\text{tol}} = 10^{-8}. \quad (\text{A7})$$

Although slightly slower than closed-form or Newton-type approaches, this method is more robust in high- Γ flows with strong shear and is well suited for producing smooth SRHD backgrounds for radiative post-processing.

A.4. Floors and ceilings

To prevent numerical vacuum states and other unphysical conditions, we enforce the following floors on primitive variables at each time step:

$$\rho \geq \rho_{\text{floor}}, \quad p \geq p_{\text{floor}}, \quad (\text{A8})$$

where ρ_{floor} and p_{floor} are chosen based on the minimum physical scales of the ambient medium. We also impose an upper bound on the sound-speed squared,

$$c_s^2 \leq c_{s,\text{max}}^2 < 1, \quad (\text{A9})$$

to ensure physical characteristic speeds and numerical stability.

We emphasize that these floors and ceilings are activated only in extremely low-density regions or near numerical boundaries, and do not qualitatively affect the jet core structure or the subsequent photospheric radiative-transfer results. Their primary role is to maintain a smooth and usable background throughout long-term evolution.